

## Equatorial Superrotation and Barotropic Instability: Static Stability Variants

G. P. WILLIAMS

*NOAA/Geophysical Fluid Dynamics Laboratory, Princeton University, Princeton, New Jersey*

(Manuscript received 14 June 2005, in final form 6 December 2005)

### ABSTRACT

Altering the tropospheric static stability changes the nature of the equatorial superrotation associated with unstable, low-latitude, westerly jets, according to calculations with a dry, global, multilevel, spectral, primitive equation model subject to a simple Newtonian heating function. For a low static stability, the superrotation fluxes with the simplest structure occur when the stratospheric extent and horizontal diffusion are minimal. Barotropic instability occurs on the jet's equatorward flank and baroclinic instability occurs on the jet's poleward flank. Systems with a high static stability inhibit the baroclinic instability and thereby reveal more clearly that the barotropic instability is the primary process driving the equatorial superrotation. Such systems produce a flatter equatorial jet and also take much longer to equilibrate than the standard atmospheric circulation.

### 1. Introduction

According to a previous numerical modeling study (Williams 2003c), certain low-latitude westerly jets can develop a barotropic instability that leads to a superrotating westerly current at the equator. The associated meridional eddy momentum fluxes, however, have a complex three-part structure due to the combined effects of the barotropic instability of the jet's equatorward flank and the baroclinic instability of the jet's poleward flank. In addition, the stratosphere limits the full development of the superrotation. Nevertheless, superrotation appears to be a natural state, particularly at low rotation rates, no matter where the jet lies.

To further define the processes involved, we now seek other examples of superrotation, preferably simpler but not necessarily more feasible. To develop such states, the stratospheric thickness is reduced and the tropospheric static stability is varied from a standard low value through medium to high values. The high static stability eliminates or severely reduces the baroclinic instability, thereby revealing more clearly the action of the barotropic instability. The circulations are again developed numerically using a global, multilevel,

spectral, primitive equation model subject to a simple Newtonian heating function that represents a linear relaxation to a specified temperature field.

The earliest studies of superrotation were primarily motivated by the need to explain the equatorial westerly jets observed in the atmospheres of Jupiter and Saturn. To begin with, a barotropic model with a tropical eddy forcing was used to show that an equatorial superrotation can be produced for both terrestrial and Jovian systems (Williams 1978, Figs. 11 and 18). Further calculations using a terrestrial general circulation model (GCM) with a standard physics formulation reveal that an equatorial superrotation is naturally prevalent at both higher and lower rotation rates for moist atmospheres but only at lower rotation rates for dry atmospheres (Williams and Holloway 1982, Fig. 1; Williams 1988, Figs. 2 and 16).

More specifically, terrestrial studies using idealized two-level models indicate that an equatorial superrotation can also exist when a sufficiently strong, zonally asymmetric (wavenumber 2) tropical heating anomaly is added to the standard axisymmetric thermal forcing (Suarez and Duffy 1992; Saravanan 1993). Additional studies of the tropical circulation with a moist aquaplanet GCM<sup>1</sup> reveal that adding a similar heating

---

*Corresponding author address:* Dr. G. P. Williams, NOAA/GFDL, Princeton University, P.O. Box 308, Princeton, NJ 08542-0308.

E-mail: Gareth.Williams@noaa.gov

---

<sup>1</sup> That is, a model with realistic radiative heating, moist convection, and a simplified global ocean surface with preassigned surface temperatures.

anomaly to the sea surface temperature can also produce an equatorial superrotation (Hoskins et al. 1999). More recent studies with a multilevel version of the Suarez–Duffy–Saravanan system confirm that an equatorial superrotation can indeed persist but only if the heating is sufficiently symmetric about the equator (Kraucunas and Hartmann 2005).

The planetary and terrestrial studies of Williams (2003a,b,c) do not invoke a longitudinal heating anomaly but instead depend on the instability of a low-latitude jet to provide the eddy driving of the superrotation. In the terrestrial calculations (Williams 2003c) with the dynamical core of a GCM, the superrotation can be produced by the barotropic instability of a jet's equatorward flank, provided that the jet lies well within the subtropics. Such a subtropical jet is produced by a Newtonian heating function that varies steeply as  $\cos^{16}\phi$  in latitude.<sup>2</sup> Similar calculations with a simpler Boussinesq primitive equation model show that superrotation is also possible with a more moderate  $\cos^8\phi$  latitudinal heating profile (Williams 2003a, Fig. 18).

In the Jovian calculations, the Boussinesq model can produce a superrotation for different vertical structures, with the active layers ranging from shallow (oceanlike) to intermediate to deep (Williams 2003a, Fig. 3f; Williams 2003b, Fig. D1), provided that an extra source of baroclinicity exists to produce an unstable jet in low latitudes. As regards the dynamics of the Jovian circulation as a whole, Vasavada and Showman (2005) provide a comprehensive review of the current status of both observation and theory.

Finally, in a novel analysis, Shell and Held (2004) explain the transition from the standard to the superrotating state in terms of a heuristic axisymmetric shallow-water model. This model represents the equatorial eddy fluxes by a confined  $\cos^{30}\phi$  torque whose implementation leads to a cubic equation defining multiple flow equilibria. Solutions to the equation show that an abrupt transition to a superrotating state occurs if the torque is strong enough. The behavior of this and the other models leads to the conclusion that superrotation is a basic mode that may be activated by a variety of eddy sources.

The presentation begins in section 2 with a brief discussion of the numerical model and parameters, followed in section 3 by a description of the solutions for the low and high static stabilities. The implications of the solutions are discussed in the concluding section 4.

## 2. Numerical model

### a. System of equations

The numerical model is based on the dynamical core of the Geophysical Fluid Dynamics Laboratory's spectral GCM and is driven by a simple heating function, along the lines devised by Held and Suarez (1994). The primitive equations have the standard hydrostatic, vorticity–divergence form that is preferred for the semi-implicit, spectral transform scheme as summarized by Gordon and Stern (1982). The model predicts the zonal, meridional, and vertical velocity components ( $u$ ,  $v$ ,  $\omega$ ), plus the temperature and surface pressure fields ( $T$ ,  $p_*$ ), as a function of the latitude, longitude, and sigma coordinates ( $\phi$ ,  $\lambda$ ,  $\sigma$ ), where  $\sigma = p/p_*$  is the normalized pressure. The variable  $\psi(\phi, \sigma) = -\int \bar{v} \cos\phi \, d\sigma$  defines a quasi-streamfunction for the zonally averaged meridional motion.

As well as a heating function, the equations include  $\nabla^8$  diffusion terms<sup>3</sup> in the horizontal and, in the vertical, a linear boundary layer drag of the form

$$\frac{\partial[u, v]}{\partial t} \dots = -k_V(\sigma)[u, v], \quad (1)$$

$$k_V = k_f \max\left(0, \frac{\sigma - \sigma_b}{1 - \sigma_b}\right), \quad (2)$$

where  $k_V^{-1}$  and  $\sigma_b$  define the time scale and the extent of the mixing. Topography, moisture, vertical diffusion, and convective adjustment are all omitted. The numerical procedure uses a triangular truncation at wavenumber 42 in the horizontal with 30 equally spaced  $\sigma$  levels in the vertical.

### b. Heating function

All flows are developed from an isothermal state of rest and are maintained by a Newtonian heating function of the form

$$\frac{\partial T}{\partial t} \dots = -k_T(\phi, \sigma)[T - T_r(\phi, p)], \quad (3)$$

where the heating rate is proportional to the difference between the atmospheric temperature and a specified radiative relaxation temperature  $T_r$  with a relaxation damping rate  $k_T(\phi, \sigma)$ . The following distribution

<sup>2</sup> At low rotation rates superrotation is actually the preferred state and occurs for the standard  $\cos^2\phi$  heating profile.

<sup>3</sup> A biharmonic diffusion was used in the previous calculations (Williams 2003c).

$$T_r = \max \left\{ T_s, \left[ T_0 - (\Delta_H T) \sin^n \phi - (\Delta_V \Theta) \log \left( \frac{p}{p_0} \right) \right] \times \left( \frac{p}{p_0} \right)^\kappa \right\} \quad (4)$$

provides the heating, where  $T_0$  and  $T_s$  are the tropospheric and stratospheric reference temperatures, respectively. The constants  $\Delta_H T$  and  $\Delta_V \Theta$  define the amplitude of the horizontal temperature and vertical potential temperature gradients. Note that, unlike Held and Suarez (1994),  $\Delta_V \Theta$  is not modified by a function of latitude. The resulting constant static stability eliminates small-scale convection at all latitudes, leading to cleaner solutions. In addition, the baroclinic zone is located in low latitudes by using a high value for the  $n$  power in (4).

### c. Parameter values

The fixed physical parameters needed in the calculations use the following standard values:  $a = 6370 \times 10^3$  m and  $\Omega = 7.292 \times 10^{-5} \text{ s}^{-1}$  for the planetary radius and rotation rate;  $g = 9.8 \text{ m s}^{-2}$  for the acceleration of gravity;  $c_p = 1004 \text{ J kg}^{-1} \text{ K}^{-1}$  for the specific heat of air;  $\kappa \equiv R/c_p = 2/7$ , where  $R$  is the gas constant;  $p_0 = 1000$  mb for a mean surface pressure based on the total mass  $p_0/g$ ; and  $T_0 = 315 \text{ K}$  and  $T_s = 150 \text{ K}$  for the reference temperatures. The other parameters are  $\sigma_b = 0.7$ ,  $(k_f, k_T) = (1, 1/40) \text{ day}^{-1}$ ,  $\Delta_H T = 40 \text{ K}$ , and  $\Delta_V \Theta = (10, 20, 40, 60, 80, 100) \text{ K}$ .

Only two cases, A and B, are presented for systems with low and high static stabilities, as given by the two values of  $\Delta_V \Theta = 10$  and  $80 \text{ K}$ , respectively. Other cases with  $\Delta_V \Theta$  values lying between these two extremes exhibit intermediate characteristics, so are not presented. Equilibration takes longer for low-latitude jets and for higher static stabilities, so these two cases have to be extended to 3000 and 9000 days, respectively.<sup>4</sup> Setting  $T_s = 150 \text{ K}$  gives a minimal stratosphere, which helps to give simpler circulations—particularly eddy momentum fluxes. To ensure that all flows lie well within the superrotation regime, the  $n$  power is set at 32; see Williams (2003c) for a discussion of the regime dependence on this parameter.

In presenting the solutions, the fields shown are time-averaged quantities, based on zonal means sampled once a day over the last 200 days of the calculations.<sup>5</sup> For brevity and clarity, the main jet and equatorial

westerly are sometimes referred to using the  $W_1$  and  $W_0$  symbols, respectively.

### d. Analysis functions

The solutions are described using standard analysis procedures and notation, with the overbar and prime denoting the zonal mean and eddies. In particular, the Eliassen–Palm (EP) flux vector  $\mathbf{F} = \{F^{(\phi)}, F^{(p)}\}$  and its scaling, together with the flux divergence  $E$ , are defined following Edmon et al. (1980) as

$$F^{(\phi)} = (-\overline{u'v'}) \frac{\cos^2 \phi}{a}, \quad (5)$$

$$F^{(p)} = \left( f \frac{\overline{v'\theta'}}{\theta_p} \right) \cos^2 \phi, \quad (6)$$

$$E = \frac{\partial F^{(\phi)}}{\partial \phi} + \frac{\partial F^{(p)}}{\partial p}, \quad (7)$$

for the dominant geostrophic components, where  $f = 2\Omega \sin \phi$ . Additional analysis with the ageostrophic terms included in (5) and (6) revealed little difference, so the terms are omitted for simplicity.

The mean quasigeostrophic potential vorticity gradient is defined, again following Edmon et al. [1980, Eq. (3.8)], on normalizing by  $2\Omega$ , as

$$q_\phi = \cos \phi + \frac{\bar{\zeta}_\phi}{2\Omega} + \sin \phi \left\{ \frac{\bar{\theta}_\phi}{\bar{\theta}_p} \right\}, \quad (8)$$

where  $\bar{\zeta} = -(a \cos \phi)^{-1} (\overline{u \cos \phi})_\phi$  is the mean relative vorticity. The condition for inertial instability

$$f(f + \bar{\zeta}) < 0 \quad (9)$$

is also calculated, but such an instability is never realized. Although the quasigeostrophic approximation is less accurate in low latitudes, the diagnostics remain useful as the barotropic component and planetary wave fluxes dominate near the equator.

## 3. Superrotating states

To examine how the static stability influences the superrotation form, we first show how a low vertical gradient ( $\Delta_V \Theta = 10 \text{ K}$ ) and a cooler stratosphere ( $T_s = 150 \text{ K}$ ) result in a simpler circulation, as defined by the  $\overline{u'v'}$  flux, etc., than that obtained in Williams (2003c). Then we examine how a high vertical gradient ( $\Delta_V \Theta = 80 \text{ K}$ ) inhibits the baroclinic instability and reveals the dominant barotropic instability as the cause of the superrotation. The intermediate states are also discussed. The dynamical behavior is also examined using the

<sup>4</sup> The standard system with  $n = 2$  takes 1000 days to equilibrate.

<sup>5</sup> Differences between the Northern and Southern Hemispheres provide a measure of the sampling limitations.

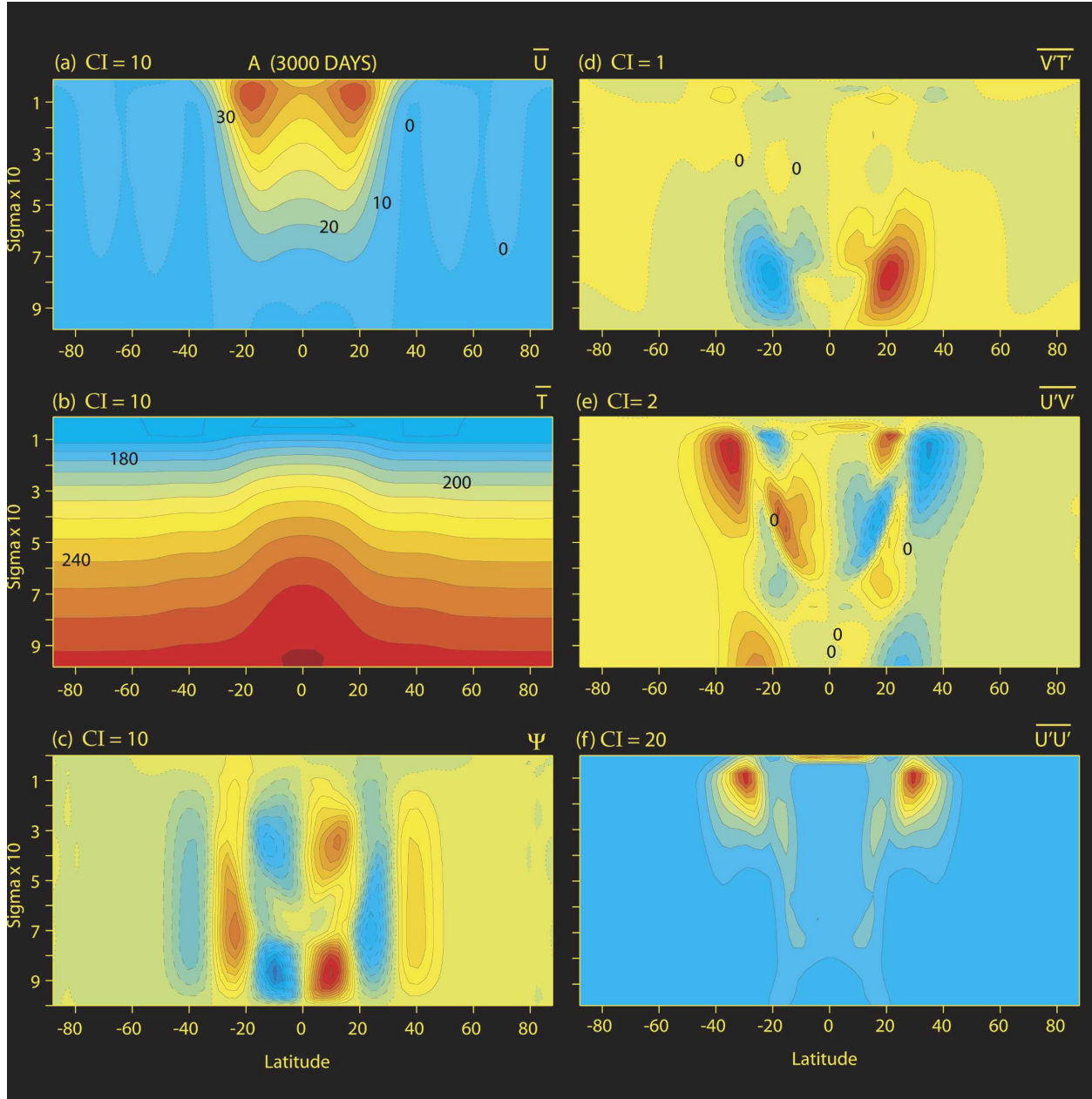


FIG. 1. Meridional sections of the primary mean and eddy fields for the case A with  $\Delta_V\Theta = 10$  K averaged over 2800–3000 days, an equilibrated phase. Labels at the top of each panel indicate the field depicted. The contour intervals (CI) are (a)  $10 \text{ m s}^{-1}$ , (b)  $10 \text{ K}$ , (c)  $10 \text{ m}^2 \text{ s}^{-2}$ , (d)  $1 \text{ K m s}^{-1}$ , (e)  $2 \text{ m}^2 \text{ s}^{-2}$ , (f)  $20 \text{ m}^2 \text{ s}^{-2}$ . The negative (zero) contours are dashed (dotted).

standard Eliassen–Palm, quasigeostrophic potential vorticity, and spectral diagrams.

#### a. Superrotation at low static stability

Case A, for  $\Delta_V\Theta = 10$  K in Fig. 1, takes 2000 days to equilibrate to a jet with  $W_1 = 100 \text{ m s}^{-1}$  and a strong equatorial westerly with  $W_0 = 69 \text{ m s}^{-1}$ . The solution differs from its predecessor (case B in Williams 2003c)

due to differences in the values of the static stability and baroclinicity, the use of a  $\nabla^8$  horizontal diffusion, and the presence of a shallower stratosphere. The Hadley cell is particularly novel in that it splits into two vertical components, thereby altering the influence of the surface drag on the zonal flow. Otherwise, the Ferrel cell and a second direct cell at  $40^\circ$  latitude coincide with the baroclinic instability as usual.

The poleward eddy heat transport,  $\overline{v'T'}$  produced by the baroclinic instability, extends from the equator to  $40^\circ$  latitude while being confined to the lower atmosphere and peaking at  $\phi = 20^\circ$  and  $\sigma = 0.8$  (Fig. 1d). The eddy momentum transport,  $\overline{u'v'}$ , is again made up of three primary components per hemisphere, consisting of a deep equatorward flux on the jet's poleward flank, a midlevel equatorward flux on the jet's equatorward flank, and a weak split poleward flux in between (Fig. 1e). According to the cospectra (in Fig. 5), these components are associated with both baroclinic and barotropic instabilities, but at different wavenumbers—see section 3d. The midlevel equatorward flux, extending over  $\phi = 0^\circ$ – $20^\circ$  and  $\sigma = 0.2$ – $0.7$ , acts to produce and maintain the equatorial superrotation. The poleward flux, however, intervenes less than in the predecessor case, and this results in the simpler form being sought. In addition, according to the  $\overline{u'u'}$  energy field, the eddies are strongest on the jet's poleward flank at the tropopause.

#### b. Superrotation at high static stability

The character of the case B flow for a high static stability ( $\Delta_V\Theta = 80$  K) changes with time, so we document both the early growth phase at 1000 days and the equilibrated phase at 9000 days (Figs. 2 and 3). This system takes much longer (8000 days) to equilibrate, presumably because of the absence of any vigorous mixing by the baroclinic instability. Between 1000 and 9000 days the  $W_1$  and  $W_0$  westerlies go from 108 and 51  $\text{m s}^{-1}$  to 241 and 232  $\text{m s}^{-1}$ , respectively, so the latitudinal jet profile becomes much flatter with time.

At 1000 days, the barotropic instability is clearly responsible for the equatorial westerly as the baroclinic instability, measured by the poleward  $\overline{v'T'}$  flux, is very weak, Fig. 2d. The equatorward, countergradient  $\overline{v'T'}$  flux in the middle and upper troposphere is significant and forced by the barotropic instability. The meridional circulation is relatively simple and consists of just a Hadley cell, though one that has two vertical components. The  $\overline{u'v'}$  flux is also simple and equatorward with two strong low-latitude components at the upper and middle levels ( $\sigma = 0.15$  and  $0.45$ ), both associated with the barotropic instability, together with a weaker mid-latitude component at low level ( $\sigma = 0.7$ ), associated with the weak baroclinic instability (Fig. 2e). The first two, large-scale components, however, occur at zonal wavenumber  $k = 3$  (Fig. 5b), while the third, medium-scale component occurs at  $k = 9$  (not shown). According to the  $\overline{u'u'}$  field the strongest eddies now occur right at the equator.

By 9000 days (see Fig. 3), the system has equilibrated with the Hadley cell being further confined to the lower

troposphere. The  $\overline{v'T'}$  flux component associated with the barotropic instability has weakened and reversed sign, whereas the component associated with the weak baroclinic instability has strengthened. The two upper-level  $\overline{u'v'}$  flux components (due to barotropic instability) merge and weaken, while the lower level component (due to baroclinic instability) increases. According to the  $\overline{u'u'}$  field, strong large-scale ( $k = 2$ , not shown) eddies occur at the equator, while two sets of medium-scale ( $k = 7$ , not shown) eddies occur in low latitudes, at  $\phi = 15^\circ$  and  $30^\circ$ .

From the growth and equilibration states of case B in Figs. 2 and 3, we conclude that the barotropic instability acts to generate and maintain the superrotation. The instability gradually weakens and the zonal flow's latitudinal profile becomes flatter near the equator as equilibrium is approached.

#### c. Superrotation variability

Calculating additional cases with  $\Delta_V\Theta = 20, 40, 60,$  and  $100$  K shows that only the first of these cases resembles the low static stability case A in its eddy fluxes; the three other cases more closely resemble the high static stability case B, with the influence of the barotropic instability over the baroclinic instability progressively increasing. As a result, the case with  $\Delta_V\Theta = 40$  K takes 7000 days to equilibrate and produces zonal flows with  $W_1 = 196$   $\text{m s}^{-1}$  and  $W_0 = 187$   $\text{m s}^{-1}$ . Thus the superrotation form seen in case B is quite general and does not need an extreme value of the static stability to be realized, though higher values do help reveal the cause of the equatorial westerly.

#### d. Superrotation dynamics

All of the above eddy fluxes appear to have forms consistent with the theories describing nonlinear baroclinic instability, barotropic instability, and Rossby wave propagation. Consequently, the EP cross sections in Fig. 4 give further insight into how the eddies originate and function in the superrotating flows. According to theory, the  $E$  flux divergence provides a measure of the source and magnitude of the transient and irreversible eddy processes, as well as the eddy forcing of the zonal mean circulation. The  $\mathbf{F}$  flux vectors give a measure of the wave propagation from one location to another.

To identify the sources of the eddies, we also examine the mean quasigeostrophic potential vorticity gradient  $\bar{q}_\phi$  as defined in (8). We recall that the equation for the eddy potential enstrophy on a quasigeostrophic beta plane with lateral coordinate  $y$  may be written as

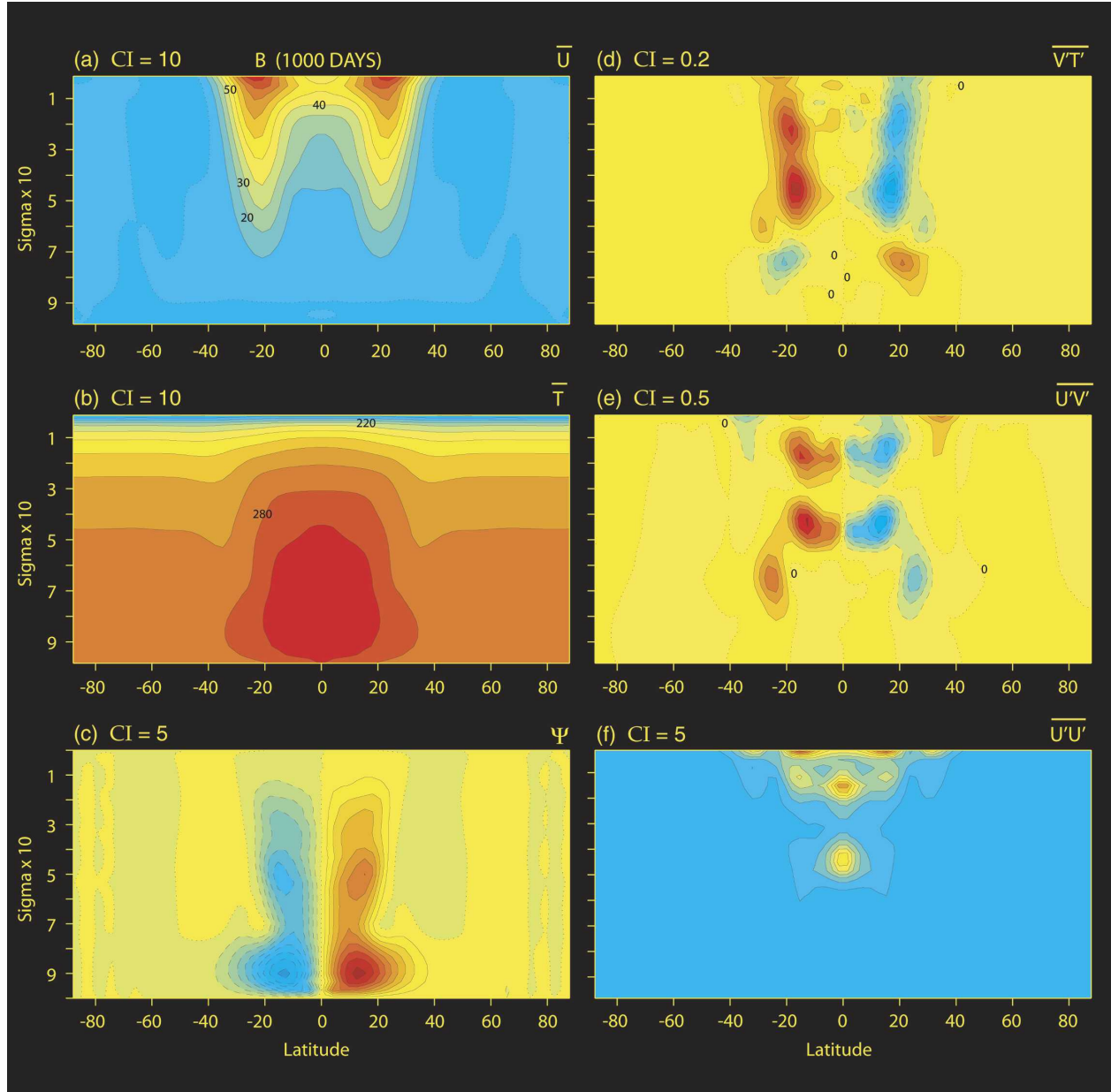


FIG. 2. Meridional sections of the primary mean and eddy fields for the case B solution with  $\Delta_v\Theta = 80$  K averaged over 800–1000 days, a growth phase. Labels at the top of each panel indicate the field depicted. The CI are (a)  $10 \text{ m s}^{-1}$ , (b)  $10 \text{ K}$ , (c)  $5 \text{ s}^{-1}$ , (d)  $0.2 \text{ K m s}^{-1}$ , (e)  $0.5 \text{ m}^2 \text{ s}^{-2}$ , (f)  $5 \text{ m}^2 \text{ s}^{-2}$ ; negative (zero) contours are dashed (dotted).

$$\frac{1}{2} \overline{(q')_t^2} + (\nabla \cdot \mathbf{F}) \overline{q_y} = \overline{S'q'}, \quad (10)$$

where  $E = \nabla \cdot \mathbf{F} = \overline{v'q'}$ , and  $S$  represents the nonconservative processes. Wave sources (instabilities) are expected to occur where  $\overline{q_y}$  has the opposite sign to  $E$ .

For case A during the equilibrated phase, the main  $E$  flux divergence and convergence regions (associated with the baroclinic instability and the vertical wave

propagation) lie mainly in the lower half of the troposphere (Fig. 4a). Their  $\mathbf{F}$  flux vectors are upward with a slight poleward tilt, then turn equatorward at mid-height, and gradually descend into the subtropics. In upper levels and at low latitudes, however, the EP fluxes are quite different, with the  $\mathbf{F}$  flux vectors mainly pointing poleward. A weak but effective divergent  $E$  flux forms over the equator in the upper troposphere in keeping with the eddy forcing of the  $W_0$  current. The  $\mathbf{F}$

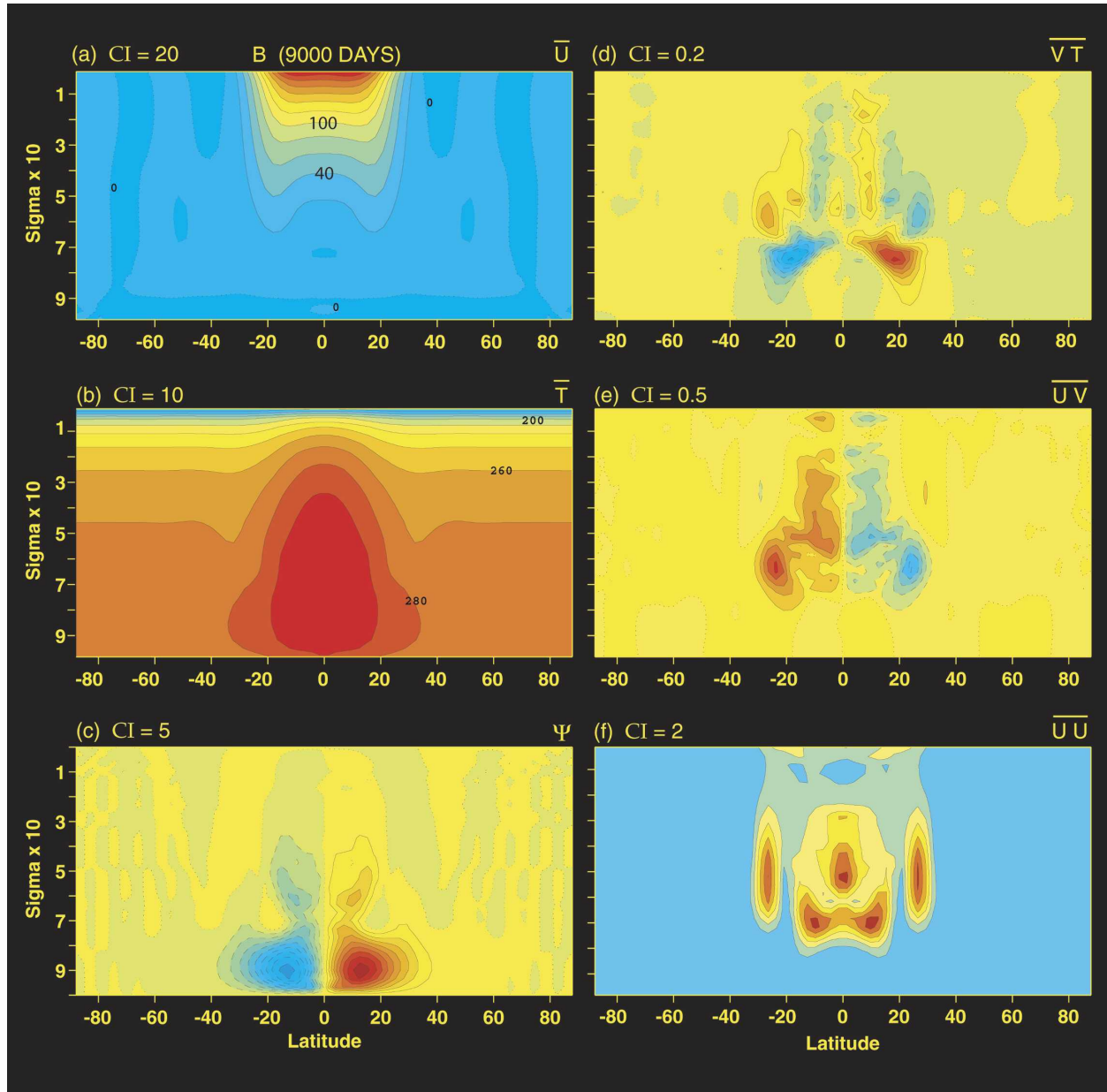


FIG. 3. Meridional sections of the primary mean and eddy fields for the case B solution with  $\Delta_v\Theta = 80$  K averaged over 8800–9000 days, an equilibrated phase. Labels at the top of each panel indicate the field depicted. The CI are (a)  $20 \text{ m s}^{-1}$ , (b)  $10 \text{ K}$ , (c)  $5 \text{ s}^{-1}$ , (d)  $0.2 \text{ K m s}^{-1}$ , (e)  $0.5 \text{ m}^2 \text{ s}^{-2}$ , (f)  $2 \text{ m}^2 \text{ s}^{-2}$ ; negative (zero) contours are dashed (dotted).

flux vectors are consistent with the action of a tropical instability that generates the large-scale waves that extend aloft from the equator to about  $20^\circ$  latitude. A secondary divergent  $E$  flux also forms at the tropopause at  $30^\circ$  and is also associated with poleward pointing  $\mathbf{F}$  flux vectors.

The EP fields for case B differ in detail but not in effect between the growth and equilibrated phases (Figs. 4b,c); they primarily reflect the changes seen in

the  $\overline{u'v'}$  fields of Figs. 2e, 3e. At 1000 days, the divergent  $E$  flux and the weak poleward  $\mathbf{F}$  flux vectors associated with the weak baroclinic instability indicate that this process has no direct influence on the dynamics equatorward of  $15^\circ$ . The latter is determined by the two strong divergent  $E$  fluxes lying aloft over the equator that produce two distinct groups of poleward  $\mathbf{F}$  flux vectors. In other words, two barotropic instability sources at the equator produce two sets of poleward

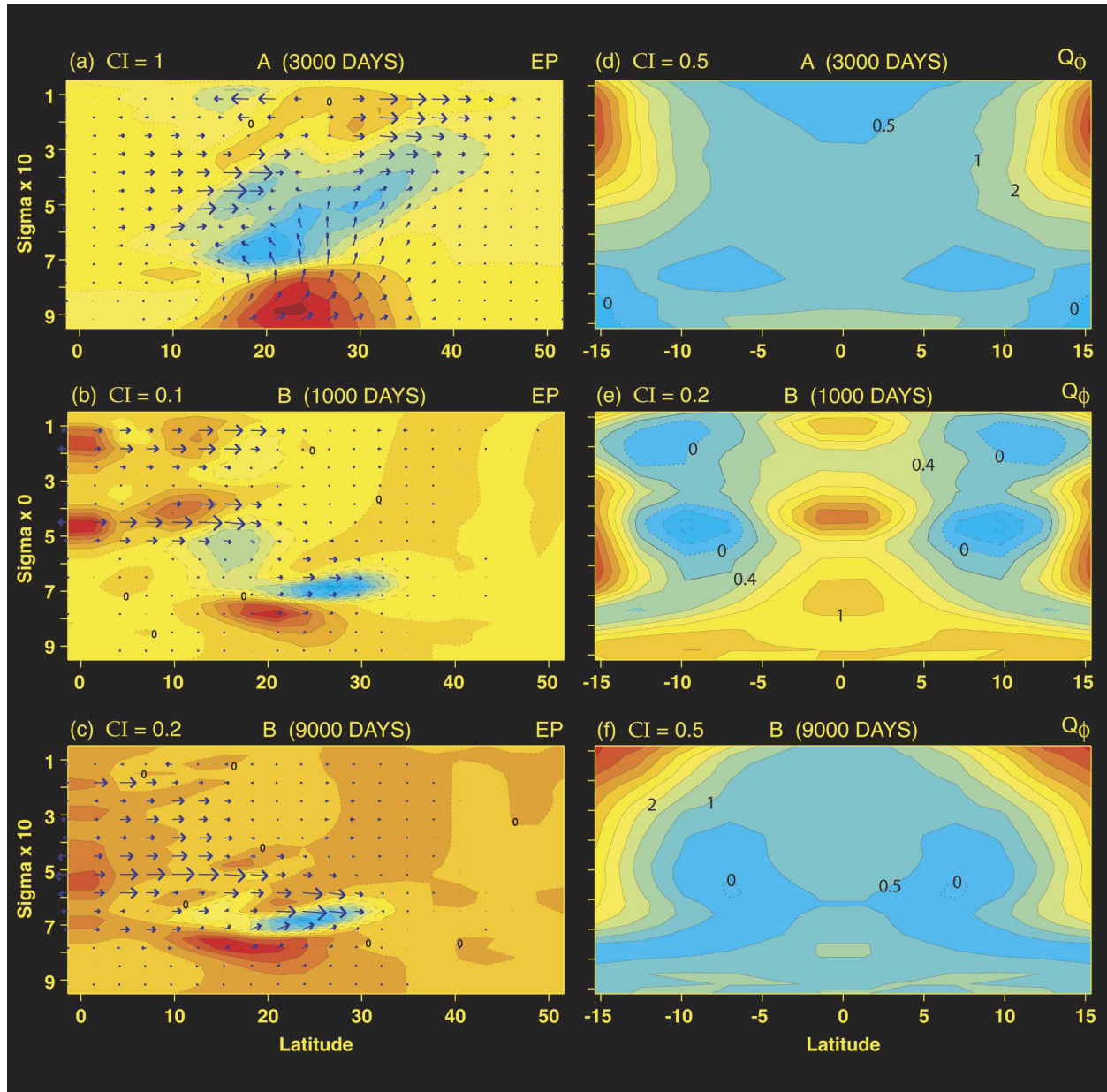


FIG. 4. Meridional sections of the geostrophic components of the Eliassen–Palm fields and the quasigeostrophic potential vorticity gradient near the equator, for case A with  $\Delta_v\Theta = 10$  K averaged over 2800–3000 days, an equilibrated phase, and for case B with  $\Delta_v\Theta = 80$  K averaged over 800–1000 days, a growth phase, and over 8800–9000 days, an equilibrated phase. The  $E$  CI are (a) 1, (b) 0.1, (c) 0.2 in units of  $10^{-5} \text{ m}^2$ . The nondimensional  $q_\phi$  contour intervals are (d) 0.5, (e) 0.2, (f) 0.5; negative (zero) contours are dashed (dotted).

propagating Rossby waves. By 9000 days, the two equatorial  $E$  fluxes have merged but are still associated with strong poleward  $F$  flux vectors, especially at middle levels. In addition, the EP fields affiliated with the baroclinic instability strengthen and indicate that the wave propagation remains poleward.

The quasigeostrophic potential vorticity gradients, defined in (8), have negative values in low latitudes during the growth stages of cases A and B—a necessary

but not sufficient condition for barotropic instability—only to be replaced by extensive regions with small or zero values as the flows equilibrate (Figs. 4d–f).

The zonal spectra for the main eddy fluxes in Fig. 5 are for the equilibrated phase of case A and the growth phase of case B. For case A, they show that the baroclinic instability occurs at a medium scale ( $k = 6$ , Fig. 5a) and the barotropic instability at a large scale ( $k = 2$ , Fig. 5b), a clear separation of scales. For case B, the

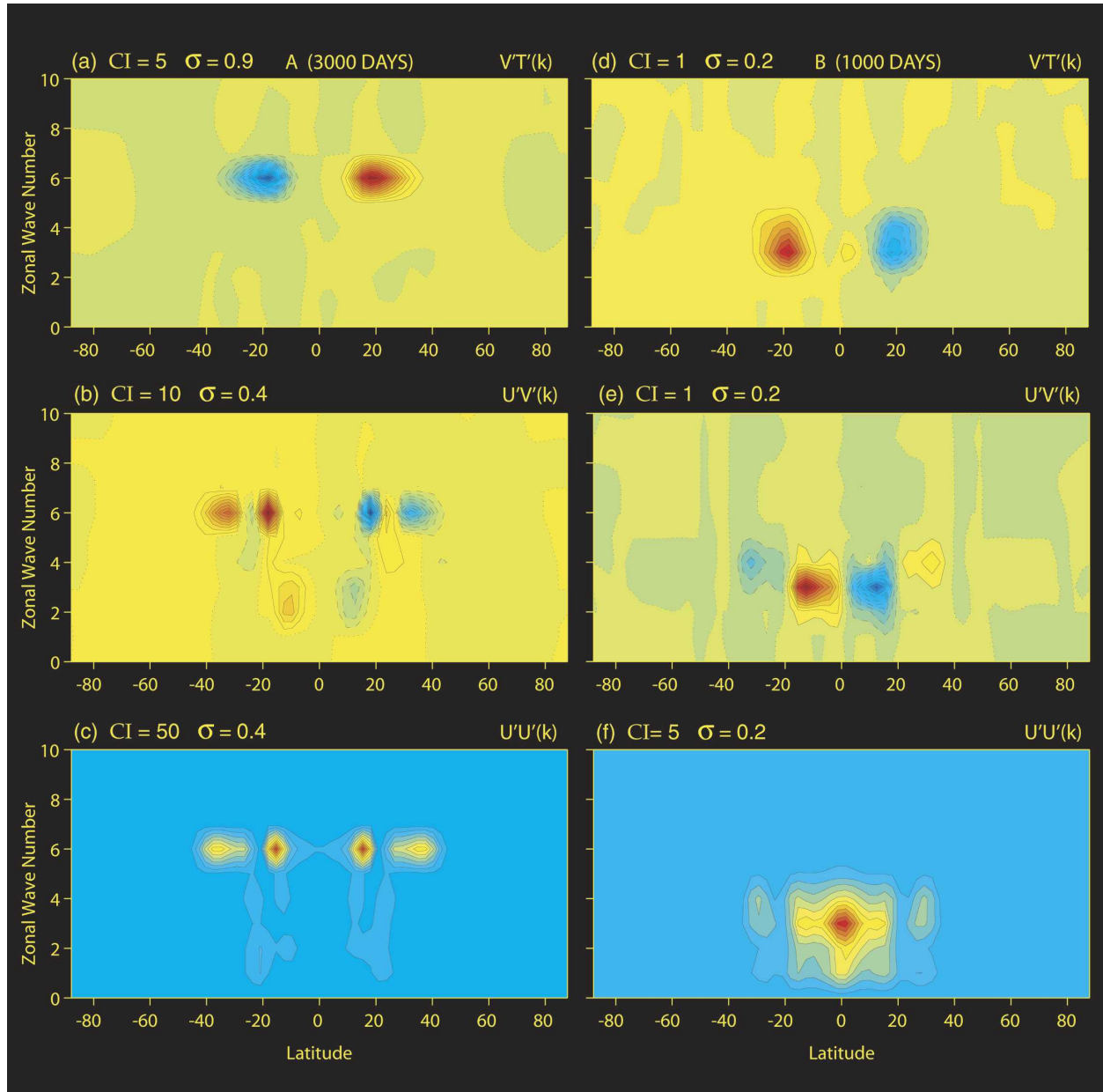


FIG. 5. Spectra of the primary eddy fluxes for case A with  $\Delta_V\Theta = 10$  K averaged over 2800–3000 days, an equilibrated phase, and for case B with  $\Delta_V\Theta = 80$  K averaged over 800–1000 days, a growth phase. The CI are (a)  $5 \text{ K m s}^{-1}$  at  $\sigma = 0.9$ , (b)  $10 \text{ m}^2 \text{ s}^{-2}$  at  $\sigma = 0.4$ , (c)  $50 \text{ m}^2 \text{ s}^{-2}$  at  $\sigma = 0.4$ . (d)  $1 \text{ K m s}^{-1}$  at  $\sigma = 0.2$ , (e)  $1 \text{ m}^2 \text{ s}^{-2}$  at  $\sigma = 0.2$ , (f)  $5 \text{ m}^2 \text{ s}^{-2}$  at  $\sigma = 0.2$ ; negative (zero) contours are dashed (dotted).

weak baroclinic instability occurs at a smaller scale ( $k = 9$ ) and a lower level ( $\sigma = 0.7$ , not shown), while the barotropic instability peaks at a smaller scale ( $k = 3$ ) and an upper level ( $\sigma = 0.2$ ), Figs. 5d–f.

#### 4. Conclusions

Two examples of systems with unstable low-latitude jets, case A with a low static stability and case B with a

high static stability, support the hypothesis that barotropic instability is the primary mechanism producing the equatorial superrotations. Increasing the static stability reduces the baroclinic instability of the jet's poleward flank, thereby allowing the barotropic instability of the jet's equatorward flank to become the dominant eddy source.

Case A exhibits a simpler, three-part  $\overline{u'v'}$  flux than that produced in previous calculations. This structural

simplification is due to differences in the static stability and baroclinicity distributions, together with the presence of a minimal stratosphere and minimal diffusion. The meridional circulation, however, is more complex, in that the Hadley cell splits in the vertical and thereby reduces the interaction between the upper and lower troposphere in low latitudes.

Case B has an even simpler, equatorward-only  $\overline{u'v'}$  flux form, one that is primarily produced by the barotropic instability. This eddy flux drives the equatorial westerly until it approaches the jet in amplitude and leads to a very flat latitudinal wind profile. Such a profile is close to the form observed on Jupiter and Saturn. The weak baroclinic instability also produces an equatorward  $\overline{u'v'}$  flux but it is located too far from the equator to influence the superrotation directly. The Hadley cell is confined to the lower atmosphere, allowing the jet to grow to values exceeding  $200 \text{ m s}^{-1}$ .

In both cases, the barotropic instability occurs at large scales ( $k = 2, 3$ ) on the equatorward flank of the jet, while the baroclinic instability occurs at medium scales ( $k = 6, 9$ ) on the poleward flank of the jet. The interaction between the two scales of the two instabilities remains undefined.

As discussed in the introduction, a superrotation can be produced in different ways. The form we have examined could be quite general in that it does not depend on the system's vertical structure and thus may actually occur on planets such as Jupiter and Saturn. However, as noted in Williams (2003c, section 6), the interpretation of the solutions may be limited by the use of conventional diagnostics. Perhaps other processes are active, particularly at lower rotation rates.

Systems with a higher static stability take longer to develop and equilibrate (up to 20 years) by a process that gradually reduces the potential vorticity gradient. Secondary calculations (not shown) with our model indicate that, if the heating is offset from the equator by  $5^\circ$ , a superrotation still occurs, but not if it is offset by  $10^\circ$ . This suggests that for Earth, the relatively rapid seasonal variations may suffice to protect the present regime from the onset of a superrotation driven slowly by the barotropic instability mechanism. However, a superrotation driven more rapidly by a large-scale longitudinal heating anomaly remains a possibility.

Additional calculations (not shown) with a moist

aquaplanet model devoid of the longitudinal thermal anomaly used by Hoskins et al. (1999) can still produce a superrotation provided the sea surface temperature varies as steeply as  $\cos^{32} \phi$  in latitude. This suggests that the moist dynamical processes associated with the Hadley cell do not eliminate the superrotation generated by the two types of forcing.

*Acknowledgments.* I thank Isaac Held for discussions on this subject, and Catherine Raphael for organizing the graphics. I am also indebted to the reviewers for suggestions that improved the presentation.

#### REFERENCES

- Edmon, H. J., B. J. Hoskins, and M. E. McIntyre, 1980: Eliassen-Palm cross sections for the troposphere. *J. Atmos. Sci.*, **37**, 2600–2616.
- Gordon, C. T., and W. F. Stern, 1982: A description of the GFDL global spectral model. *Mon. Wea. Rev.*, **110**, 625–644.
- Held, I. M., and M. J. Suarez, 1994: A proposal for the intercomparison of dynamical cores of atmospheric general circulation models. *Bull. Amer. Meteor. Soc.*, **75**, 1825–1830.
- Hoskins, B., R. Neale, M. Rodwell, and G.-Y. Yang, 1999: Aspects of the large-scale tropical atmospheric circulation. *Tellus*, **51**, 33–44.
- Kraucunas, I., and D. L. Hartmann, 2005: Equatorial superrotation and the factors controlling the zonal-mean winds in the tropical upper troposphere. *J. Atmos. Sci.*, **62**, 371–389.
- Saravanan, R., 1993: Equatorial superrotation and maintenance of the general circulation in two-level models. *J. Atmos. Sci.*, **50**, 1211–1227.
- Shell, K. M., and I. M. Held, 2004: Abrupt transition to strong superrotation in an axisymmetric model of the upper troposphere. *J. Atmos. Sci.*, **61**, 2928–2935.
- Suarez, M. J., and D. G. Duffy, 1992: Terrestrial superrotation: A bifurcation of the general circulation. *J. Atmos. Sci.*, **49**, 1541–1554.
- Vasavada, A. R., and A. P. Showman, 2005: Jovian atmospheric dynamics: An update after *Galileo* and *Cassini*. *Rep. Prog. Phys.*, **68**, 1935–1996.
- Williams, G. P., 1978: Planetary circulations: 1. Barotropic representation of Jovian and terrestrial turbulence. *J. Atmos. Sci.*, **35**, 1399–1426.
- , 1988: The dynamical range of global circulations—I. *Climate Dyn.*, **2**, 205–260.
- , 2003a: Jovian dynamics. Part III: Multiple, migrating, and equatorial jets. *J. Atmos. Sci.*, **60**, 1270–1296.
- , 2003b: Jet sets. *J. Meteor. Soc. Japan*, **81**, 439–476.
- , 2003c: Barotropic instability and equatorial superrotation. *J. Atmos. Sci.*, **60**, 2136–2152.
- , and J. L. Holloway, 1982: The range and unity of planetary circulations. *Nature*, **297**, 295–299.